Self-organized dynamics and the transition to turbulence of confined active nematics

Achini Opathalage[a,1], Michael M. Norton[a,1], Michael P. N. Juniper[a], Blake Langeslay[a], S. Ali Aghvami[a], Seth Fraden[a,2], and Zvonimir Dogic[a,b,2]

[a]Department of Physics, Brandeis University, Waltham, MA 02453; and [b]Department of Physics, University of California, Santa Barbara, CA 93106

Edited by Noel A. Clark, University of Colorado Boulder, Boulder, CO, and approved January 29, 2019 (received for review September 30, 2018)

We study how confinement transforms the chaotic dynamics of bulk microtubule-based active nematics into regular spatiotemporal patterns. For weak confinements in disks, multiple continuously nucleating and annihilating topological defects self-organize into persistent circular flows of either handedness. Increasing confinement strength leads to the emergence of distinct dynamics, in which the slow periodic nucleation of topological defects at the boundary is superimposed onto a fast procession of a pair of defects. A defect pair migrates toward the confinement core over multiple rotation cycles, while the associated nematic director field evolves from a distinct double spiral toward a nearly circularly symmetric configuration. The collapse of the defect orbits is punctuated by another boundary-localized nucleation event, that sets up long-term doubly periodic dynamics. Comparing experimental data to a theoretical model of an active nematic reveals that theory captures the fast procession of a pair of $+1/2$ defects, but not the slow spiral transformation nor the periodic nucleation of defect pairs. Theory also fails to predict the emergence of circular flows in the weak confinement regime. The developed confinement methods are generalized to more complex geometries, providing a robust microfluidic platform for rationally engineering 2D autonomous flows.

active matter | liquid crystals | topological defects | pattern formation | self-organization

Powered by the consumption of chemical energy, active nematic liquid crystals generate mesoscopic active stresses that render the entire system unstable. For extensile nematics, slight bend distortions of the director field create hydrodynamic flows that further deform the director field (1–4). Upon saturating, these distortions produce pairs of motile topological defects that drive large-scale turbulent-like dynamics (5–17). Design of active matter-based devices that directly convert chemical energy into macroscopic mechanical work requires predictive control of the emergent spatiotemporal patterns. In passive liquid crystals, such goals can be accomplished by prescribing confinement geometry and boundary anchoring conditions, which, in turn, determine the configuration of the director field throughout the sample (18–20). However, the full extent to which the dynamics of active liquid crystals can be prescribed through control of the boundaries remains an open question. For example, recent theoretical work suggests that circular confinement generates robust circular flows that are largely independent of the details of the director boundary conditions (21).

The 2D active liquid crystals studied here are formed by depositing microtubule fibers comprising individual microtubules microns in length bundled together by depletion forces on an oil–water interface. Clusters of ATP-powered kinesin motors bind to neighboring microtubules powering their sliding and generating net extensile stresses (14, 15). We confined 2D active nematics by filling photolithographically shaped holes formed in photoresist with oil and covering the oil interface with an aqueous suspension of active fibers. The nematic thus formed is a thin 2D active material with in-plane boundaries provided by the processed photoresist (Fig. 1). The hard wall boundaries enforce both the no-slip condition and the parallel anchoring that are readily described by hydrodynamic models of confined active nematics (21–26).

Below a critical confinement size, we observe self-organized circular flows, which are a ubiquitous feature of diverse experimental systems (27–31). However, experimentally identified criteria for the onset of the circular flows are different from theoretical predictions. For a subset of confinements, we observe slow and highly periodic dynamics of boundary-induced defect nucleation that is superimposed on the fast circular flows, a phenomenon we refer to as doubly periodic dynamics. Related dynamics were also observed by imposing a distinct boundary condition in which the substrate has anisotropic viscosity due to a smectic substrate (32). Taken together, these observations suggest that doubly periodic dynamics are a ubiquitous feature of confined active nematics that is not accounted for by the current theoretical models. In continuum theories of passive and active low molecular weight liquid crystals, defects can propagate through molecular reorientation, a mechanism which does not move material. In contrast, here, defects avoid crossing material lines defined by the director field because their motion is heavily constrained by the long spatial extent of the constituent

Significance

Topological defects are a ubiquitous feature of diverse materials ranging from superconductors to liquid crystals. In contrast to conventional materials where defects produce static field configurations, topological defects in energy-consuming active matter acquire motility. In bulk active nematic liquid crystals, motile defects drive turbulent-like dynamics. We show that confining a model experimental active nematic converts bulk chaotic motion into coherent circulatory flows. This observation suggests the possibility of exploiting geometric design to encode the spatiotemporal dynamics of topological defects, thereby endowing synthetic materials with the self-organized capabilities heretofore mainly found in living organisms. Furthermore, qualitative differences between experimental observations and numerical solutions of hydrodynamic equations suggest improvements to widely studied but incomplete theoretical models.

Author contributions: M.M.N., M.P.N.J., S.F., and Z.D. designed research; A.O., M.M.N., and M.P.N.J. performed research; S.A.A. contributed new reagents/analytic tools; A.O., M.M.N., M.P.N.J., B.L., and S.F. analyzed data; and A.O., M.M.N., S.F., and Z.D. wrote the paper.

The authors declare no conflict of interest.

This article is a PNAS Direct Submission.

[1]A.O. and M.M.N. contributed equally to this work.

[2]To whom correspondence may be addressed. Email: zdogic@physics.ucsb.edu or fraden@brandeis.edu.

This article contains supporting information online at www.pnas.org/lookup/suppl/doi:10.1073/pnas.1816733116/-/DCSupplemental.

Published online February 25, 2019.

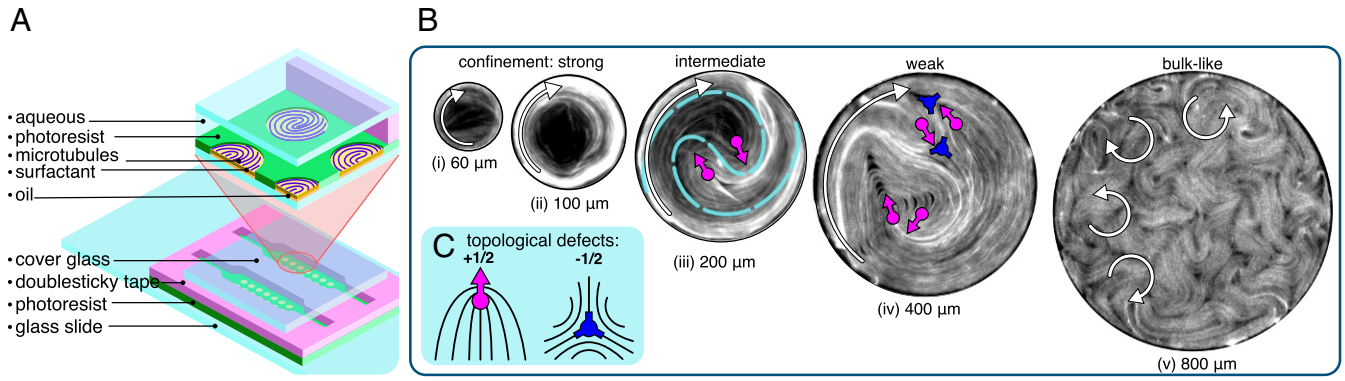

Fig. 1. Active nematics in weak, intermediate, and strong confinement regimes. (*A*) Schematic of sample cell used to confine active nematic. A micropattern of cylindrical holes was imprinted into a photoresist layer bound to a microscope slide. Oil filling the flow chamber was displaced with an aqueous active mixture, leaving behind holes with a circular oil–water interface located near the top of the cylindrical opening. Centrifuging microtubules onto the oil–water interface led to the formation of confined active nematic. (*B*) Fluorescence images of confined active nematics with diameters of (*i*) 60, (*ii*) 100, (*iii*) 200, (*iv*) 400, and (*v*) 800 μm. White arrows indicate direction of circulation. Cyan line overlaying the 200 μm disk highlights the double spiral configuration of the nematic director observed for intermediate confinements. Photographs are not to scale. (*C*) Structure of nematic director field around topological defects of charge $+1/2$ (magenta) and $-1/2$ (blue).

fibers. Our results on confined active nematics challenge existing theoretical models with experimental data, identifying physical features whose inclusion into theoretical models may reconcile the observed differences.

Experimental Results

Using microfluidic technologies, we confined active nematics into circular geometries whose diameter ranged from 60 μm to 800 μm (Fig. 1). For all confinements studied, microtubules exhibited parallel alignment to the boundaries, which ensured that the nematic director field contained topological defects. Specifically, circular geometry has an Euler characteristic of +1; thus the topological charge of all disclinations has to add up to this value (33). For the strongest confinements ranging up to 100 μm, the disk diameter was less than the defect size in a bulk nematic (Fig. 1*B*, *i* and *ii*). Defect size indicates the minimum radius of curvature that microtubule fibers can support without fragmenting; therefore, in this regime, microtubules accumulate at the boundary, leading to significant density gradients. For intermediate confinements (100 μm to 200 μm), the active nematics formed two $+1/2$ defects typically arranged into an asymmetric double spiral configuration (Fig. 1*B*, *iii*). This is distinct from passive nematics in which the director field features two static $+1/2$ defects oriented along the same line in an antipodal symmetric configuration (34, 35). For weak confinements (300 μm to 600 μm), we observed proliferation of additional defects throughout the active nematic (Fig. 1*B*, *iv*). In all three regimes, active nematics exhibited robust circular flows. Further increasing the confinement size to 800 μm and beyond yielded active nematics with turbulent bulk-like dynamics (Fig. 1*B*, *v*). The constraint that the total topological charge adds up to +1 remained intact for all confinement regimes, since nucleation events only create topologically neutral $\pm\frac{1}{2}$ defect pairs.

Intermediate Confinements. We first describe dynamics in the intermediate confinement regime, which exhibited persistent circulating flows accompanied by complex but highly periodic dynamics of topological defects (Movies S1 and S2). From a time sequence of fluorescently acquired images, we extracted the spatiotemporal evolution of the nematic director field (Fig. 2*A*), and, using a previously developed algorithm, we identified the locations of the topological defects (15). Immediately before a boundary nucleation event, the two circulating $+1/2$ defects almost merged at the center, and the director field adopted a nearly circularly symmetric configuration (-2.5 s in Fig. 2*A*). This configuration was unstable, and the effective defect merger at the confinement core coincided with initiation of a remote nucleation event at the boundary (0 s to 5 s in Fig. 2*A*). Specifically, over the next few seconds, the boundary-adjacent microtubule layer underwent a large-scale inward buckling deformation that was driven by the intrinsic bend instability of the extensile active nematics. As the instability grew, it generated a pair of $\pm\frac{1}{2}$ defects. The $+1/2$ defect was propelled toward the center, while the oppositely charged $-1/2$ defect remained at the boundary, eventually merging with one of the two original $+1/2$ defects (5 s to 10 s in Fig. 2*A*). The boundary nucleation event briefly disrupted the regular procession of the defects, but, within a short time, the active nematic reestablished the spiral configuration that powered robust circular flows. The periodicity of these flows was ~ 10 s, as can be seen by plotting the angular position of the $+1/2$ topological defects (Fig. 2*C*). Over multiple rotations, the defect pair, arranged in a double spiral, slowly migrated toward the center (Fig. 2*B*). This inward winding reconfigured the nematic director field, recreating the nearly circularly symmetric configuration (44 s in Fig. 2*A*), which initiated another boundary-induced nucleation event.

The above described periodic dynamics were coupled to spatiotemporal changes in the local microtubule density. In accordance with theory that predicts the motion of extensile active nematics from regions of high to low curvature (1, 36), the elongating microtubule fibers drove material toward the boundary, leaving the interior devoid of nematic material (Fig. 2*D*). In the subsequent cycle, the disk's center was repopulated with filaments as the $+1/2$ defect detached from the boundary and moved toward the center. This defect pulled along a bright fiber of microtubules, which served as a tracer for the deformations undergone by the nematic material elements (cyan line in Fig. 2*A*). This fiber continuously elongated, winding around the center multiple times; from 0 s to 44 s, the material element grew from a 10-μm protrusion to a several-millimeter-long coiled fiber. Notably, the two defects arranged at the core of the double spiral never crossed the elongating fiber and were directed inward in slowly collapsing orbits.

Following the system on longer time scales revealed that the above described dynamics repeated itself with a period of $\sim 40 \pm 5$ s (Fig. 3 *A* and *B*). Time evolution of the angular defect position confirmed that the slow dynamics of

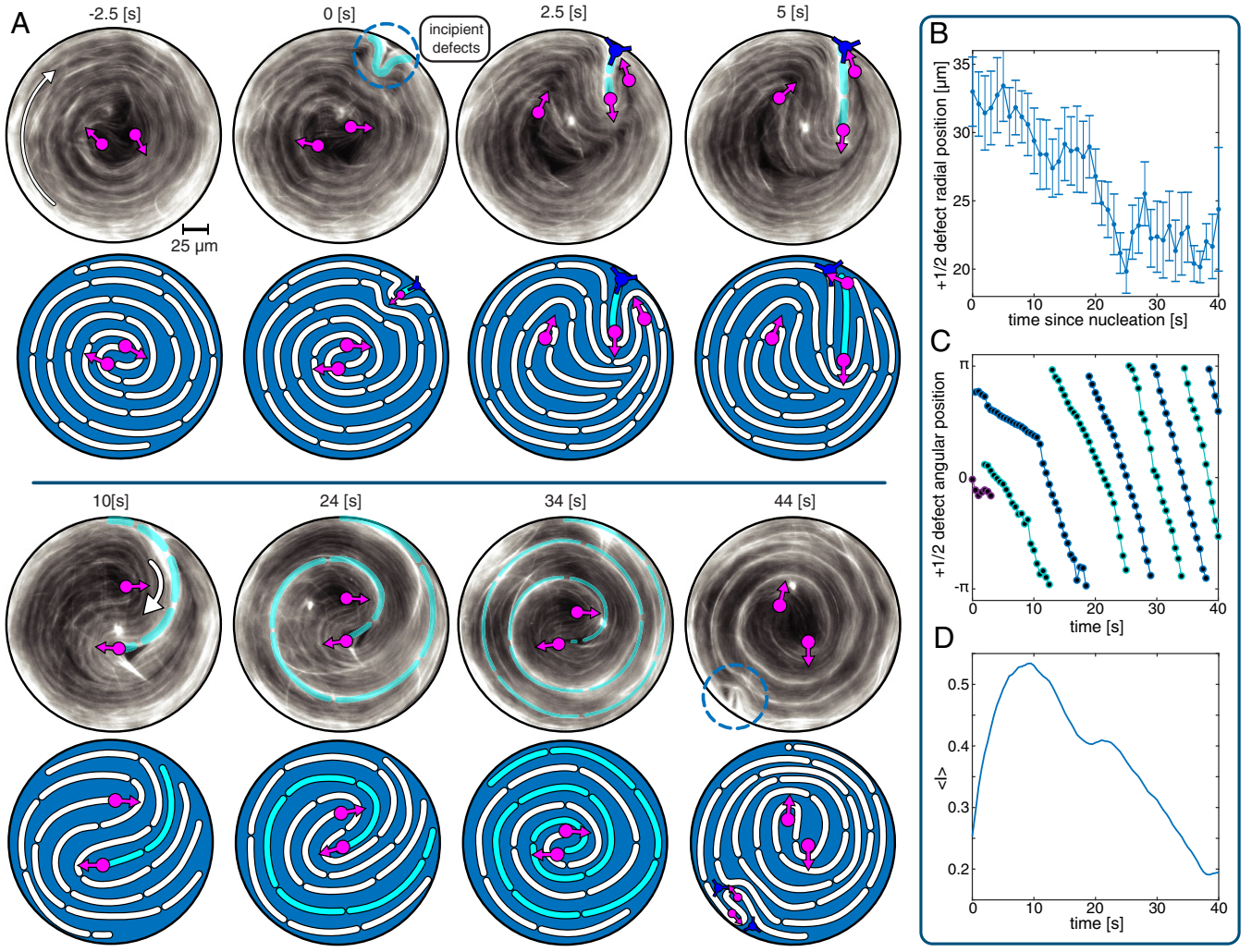

Fig. 2. Dynamics of confined active nematic at intermediate confinements. (*A*) Fluorescence images and accompanying illustrations depict the spatiotemporal evolution of the nematic field during one cycle consisting of boundary-induced defect nucleation and defect orbit collapse. At −2.5 s, the system begins with microtubules wound tightly into a spiral such that they appear to be arranged in closed, concentric circles. At 0 s, microtubules adjacent to the boundary (cyan) buckle, creating an inwardly propagating $+1/2$ defect. At 2.5 s to 5 s, a fracture forms between the $-1/2$ defect created during nucleation and one of the original $+1/2$ defects, returning the system to a two-defect configuration. At 10 s to 34 s, a pair of orbiting $+1/2$ defects approach each other over multiple rotations. At 44 s, the confined active nematic returns to the original, tightly wound and therefore almost perfectly circular configuration with weak azimuthal gradients. Over the next few seconds, the microtubule layer once again buckles. A subsequent cycle is shown in *SI Appendix*, Fig. S1, and dynamics are shown in Movie S2. (*B*) Radial position of $+1/2$ defects as a function of time shows the inward defect migration. The defect position was averaged over 20 cycles. The radial position increases toward the end of the cycle as buckling begins to push the existing defects away from the center. Error bars are SE. (*C*) Angular position of two $+1/2$ defects during one defect nucleation cycle is indicative of the fast procession with a ∼10-s period; colors indicate different defects. (*D*) Fluorescence intensity, averaged over the central area with 50-μm diameter. Defect nucleation repopulates the disk interior with microtubules for first 10 s; afterward, the microtubule density steadily decreases as the defects circulate and filaments are expelled toward the boundary (10 s to 40 s). Confinement diameter is 200 μm.

boundary-induced nucleation were superimposed on much faster circular flows, in which defects completed a circular orbit with a ∼10-s period (Fig. 3*D*). In the vast majority of cases, the boundary-induced defect nucleation preserved the existing handedness of the circular flows. However, on rare occasions, reversal of flow handedness was observed (Movie S1 at ∼4,300 s). Fast circular flows with ∼10 s periodicity were also seen in temporal evolution of the velocity fields obtained using particle imaging velocimetry (PIV) on the fluorescently labeled microtubules (Fig. 3*C* and Movie S2). However, caution needs to be taken when interpreting these results, since the PIV algorithm, which detects changes in light intensity, does not track dynamics that are tangent to uniformly aligned regions when the microtubules are densely labeled; thus such data are semiquantitative.

To gain insight into the mechanisms underlying the doubly periodic dynamics, we extracted active stresses from the evolving nematic director field. Hydrodynamic theory postulates that these stresses are proportional to the nematic order tensor $\mathbf{Q}$. Thus, the force that drives the autonomous flows is related to the gradients of the active stress, and regions of spatially varying nematic order are required to generate flows (1, 2). For extensile active nematics, these forces point from high to low curvature. An experimentally measured map of the nematic director field yields an estimate of the active force, $\propto \nabla \cdot \mathbf{Q}$, and the component of this force that drives circulating flows, $\propto \hat{\mathbf{e}}_\theta \cdot \nabla \cdot \mathbf{Q}$ (Fig. 3*E*). Our analysis assumes that activity is independent of microtubule density. The initial asymmetric spiral director field generated significant gradients of stress in the azimuthal direction, which, in turn, powered strong circular flows in the

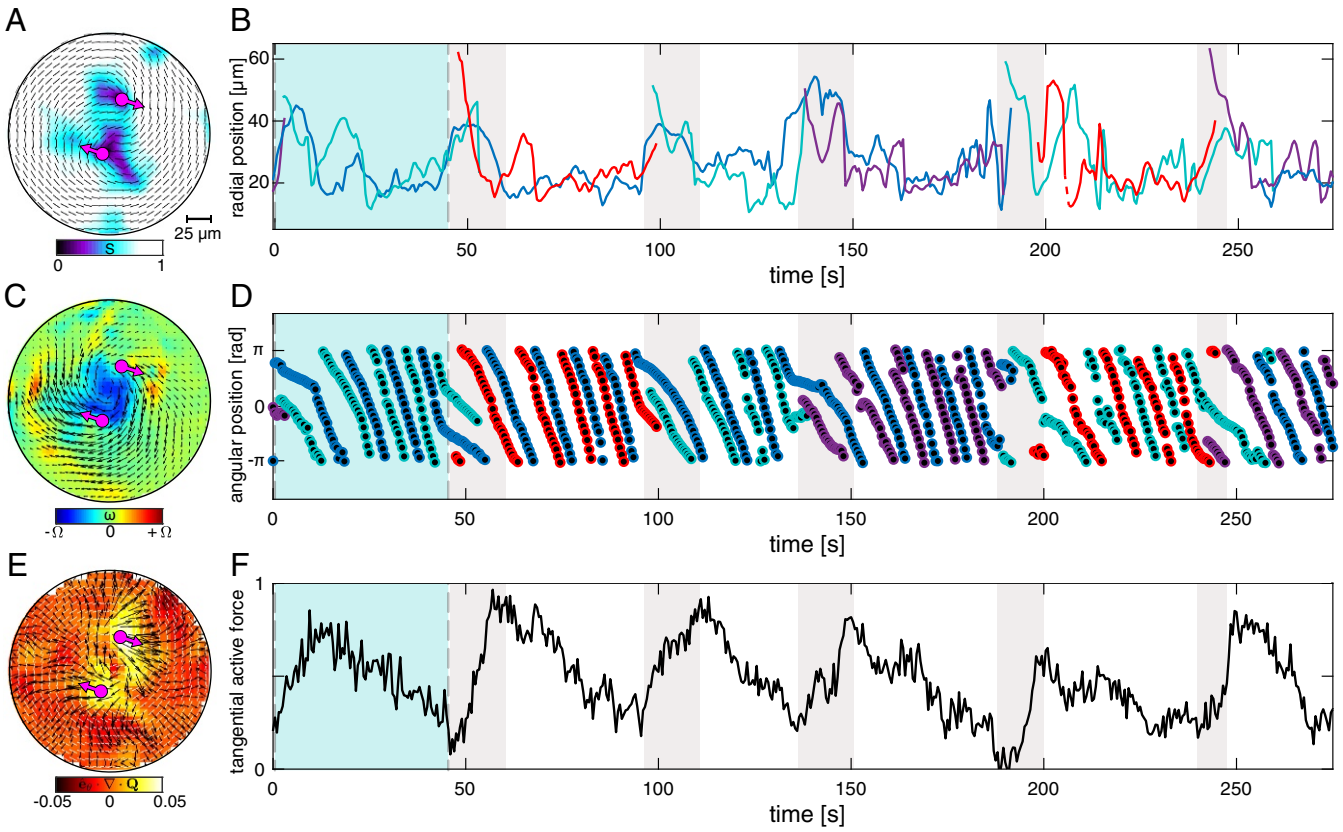

Fig. 3. Long-time doubly periodic dynamics at intermediate confinements. (*A*) Map of the director field **n** and the associated order parameter *S* extracted from the fluorescence images. Two $+1/2$ defects are also indicated with magenta arrows. (*B*) Radial position of $+1/2$ defects plotted over several boundary nucleation events (period is $\sim$50 s) and many defect orbit periods (period is $\sim$10 s). Colors indicate different defects. (*C*) PIV analysis yields the autonomous flow and the vorticity field (vorticity scale $\Omega = \pm 0.8\ s^{-1}$). (*D*) Angular position of $+1/2$ defects. The unchanging sign of the slope indicates that handedness of the circulation persists over multiple cycles of defect nucleation. Colors indicate different defects. (*E*) Spatial map of $\nabla \cdot \mathbf{Q}$ (black arrows) and the magnitude of tangential component $\hat{\mathbf{e}}_\theta \cdot \nabla \cdot \mathbf{Q}$ (color field). (*F*) Spatially integrated total active force in the tangential direction $\int d\mathbf{x}\,(\hat{\mathbf{e}}_\theta \cdot \nabla \cdot \mathbf{Q})$ as a function of time. Maxima correspond to configurations where the two $+1/2$ defects are far from one another; minima occur directly before nucleation when defects have effectively merged. Scale is normalized by 64 μm. Images in *A*, *C*, and *E* correspond to Fig. 2*A* (t = 10 s). The light blue shaded window in *B*, *D*, and *F* corresponds to snapshots in Fig. 2*A*. The gray shaded windows indicate nucleation events. Confinement diameter is 200 μm.

direction consistent with the hydrodynamic theory of extensile active nematics (Fig. 3*F*, t = 10 s). The evolution of the system toward a more tightly wound spiral reduced the magnitude of this force. The boundary-induced defect nucleation correlated with the time point where the active force in the azimuthal direction reached a minimum. This suggests that the sufficiently strong flow alignment generated by the circular flows suppressed the defect nucleation that might otherwise form through the bend instability. The boundary-induced defect nucleation could proceed only once the flows were sufficiently weak due to reconfiguration of the director field and the associated active force.

Transition to Strong Confinements. Doubly periodic dynamics associated with the intermediate confinement regime persisted as the diameter was reduced to below 200 μm. However, for 100-μm confinements, the dynamics exhibited new behaviors. In this regime, the confinement size is comparable to the defect core size (Movie S3). Consequently, microtubule accumulation along the boundary became increasingly prominent. The center of the disk, if it contained microtubules at all, exhibited simple rigid body rotation driven by the boundary. Reducing the confinement size further to 60 μm accentuated these behaviors (Fig. 4 and Movie S4). In this case, the extending fibers no longer formed a continuous nematic field, but formed a fragmented ring at the boundary, while leaving large voids in the center. The temporal dynamics were no longer continuous and regular. Despite the loss of some structural order, we still observed fairly consistent circular rotations and intermittent buckling events. It is likely that the continuum approximation is no longer valid in this limit. Theory predicts that, for small enough confinements, net circulation ceases because the active stresses are not strong enough to overcome the elastic distortions (21). We did not observe this predicted event.

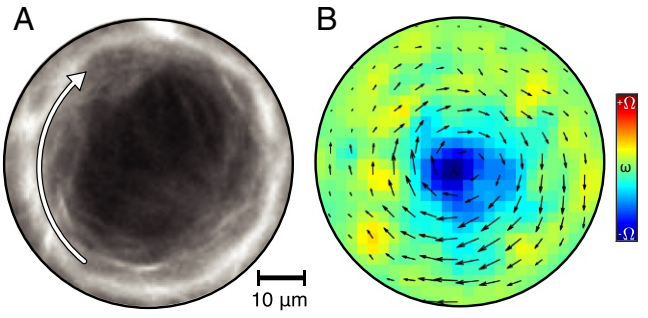

Fig. 4. Active nematics in strong confinement. (*A*) Circulating fluorescently labeled microtubules confined to a 60-μm-diameter disk (Movie S4). (*B*) Time-averaged (25 s) flow and vorticity fields (vorticity scale $\Omega = \pm 0.19\ s^{-1}$).

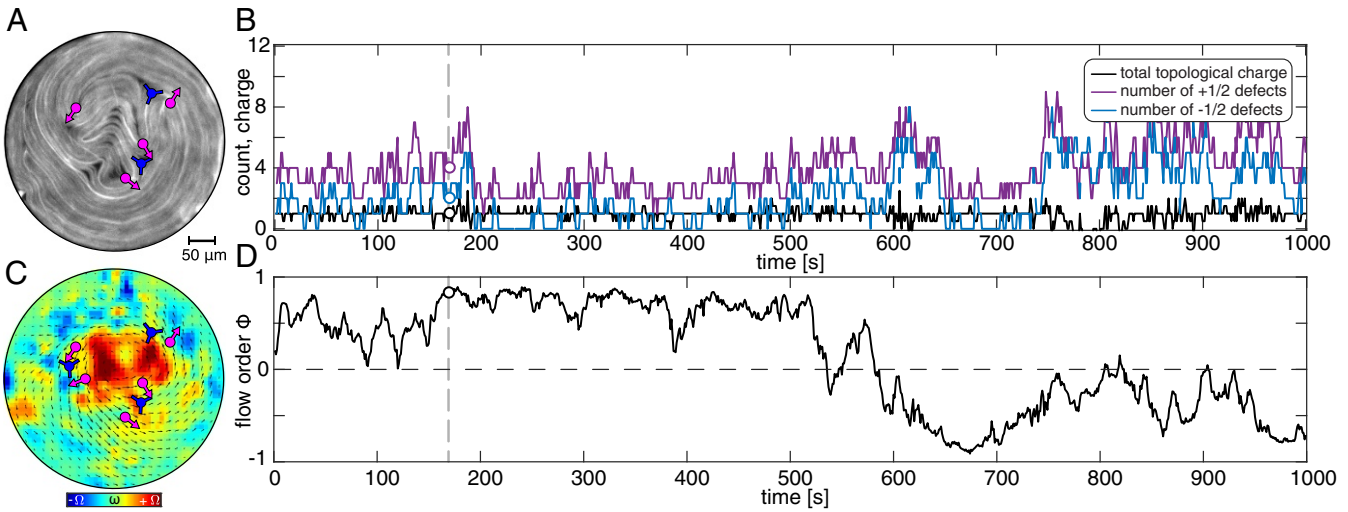

Fig. 5. Active nematics in weak confinement. (*A*) Active nematic in the regime where topological defects nucleate both in the interior and at the boundary; the $+1/2$ defects are predominantly aligned along the flow direction. (*B*) Time evolution of the number of $+1/2$ defects (magenta), $-1/2$ defects (blue), and the total topological charge (black). The total charge remains +1 except for short-time tracking errors. (*C*) Spatial map of the instantaneous flow field and vorticity (vorticity scale is $\Omega = \pm 0.27\ s^{-1}$). (*D*) Time evolution of the flow order parameter demonstrates that the circular flows with specific handedness persist for periods up to 10 min. The vertical line in *B* and *D* corresponds to the time in *A* and *C*. Confinement diameter is 400 μm.

Weak Confinements. Active nematics confined to disks with diameter between 400 μm and 600 μm exhibited qualitatively new behavior compared with the intermediate and strong confinement regimes. In this regime, defects nucleated both at the boundary and within the interior (Fig. 5*A*). In addition to the two topologically required $+1/2$ defects, at most times, the system contained several additional defect pairs, whose number fluctuated anywhere between 2 and 10 (Fig. 5*B*). Except for short-term errors in defect tracking, the net charge of all defects added up to +1. Visual inspection revealed that these samples still exhibited coherent circular flows despite the presence of additional defects (Movie S5). To quantify this phenomena, we defined the signed order parameter that indicates the degree of flow circulation as $\Phi(t) = \langle \mathbf{u} \cdot \hat{\mathbf{e}}_\theta / |\mathbf{u}| \rangle$, where $\mathbf{u}$ is the velocity field extracted from the PIV algorithm (Fig. 5*C*). $\Phi = \pm 1$ for system-scale coherent circular flows, while $\Phi = 0$ indicates lack of net transport along the azimuthal direction (25, 31). Temporal evolution of the flow order parameter confirms that weakly confined active nematics exhibited persistent circular flows that switched handedness on the time scale of tens of minutes (Fig. 5*D*).

Transition to Bulk Turbulence. So far, we described the dynamics of active nematics in confinements ranging from 60 μm to 600 μm. For intermediate confinements, dynamics consisted of periodic boundary nucleation and the slow collapse of the defect orbits superimposed on their rapid procession. Circular flows persisted for larger diameter disks in the weak confinement regime. Here defects nucleated both at the boundary and within the interior, and the nucleation dynamics were no longer deterministic but rather chaotic. The transition between these regimes was gradual. To compare the behaviors across all regimes, we plotted the time-averaged flow order parameter $\langle |\Phi| \rangle_t$ against the confinement size (Fig. 6*A*). Self-organized circular flows had the same degree of flow order for confinements up to 600 μm. Beyond this size, $\langle |\Phi| \rangle_t$ dropped to zero, indicating the transition to bulk-like chaotic dynamics (Movie S6).

Motivated by the close relationship between topological defects and autonomous flows, we examined how the defect density depends on the confinement size. In bulk active nematics, active stresses generate topological defects, and their magnitude determines the preferred defect density. Reducing the confinement diameter leads to an increase of the effective density, since topological constraints ensure formation of at least two $+1/2$ defects, even for confinements smaller than the average bulk defect spacing. Plotting the average defect density as a function of the confinement size reveals the expected increase for geometries less than ~ 200 μm (Fig. 6*A*), which is comparable to the length scale extracted from the analysis of bulk active nematics (37). Therefore, from a structural perspective, active nematics become unconfined above ~ 200-μm confinements. In contrast, the dynamical signature of confinement, as manifested by the emergence of circular flows, persists for much weaker confinement, remaining even as the diameter is increased to ~ 600 μm (Fig. 6*A*). We compared these findings to predictions of the hydrodynamic theory by determining how the defect

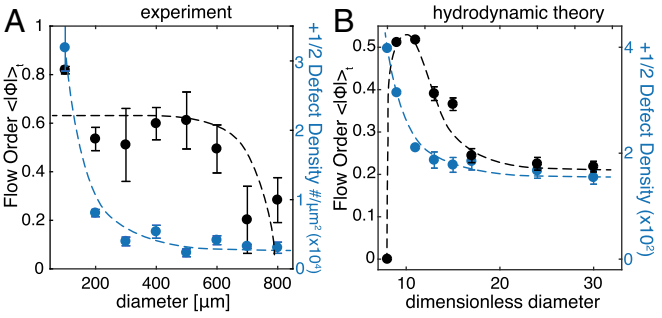

Fig. 6. Dynamical and structural criteria for the onset of circular flows. (*A*) Experimentally measured flow order parameter (black) and $+1/2$ defect density (blue) are averaged over sample lifetimes and plotted as a function of the confining disk diameter. The onset of circular flows is observed for confinements below 600 μm, while the topological constraint does not modify the average defect density until the confinement is below 200 μm. Error bars represent SE across different disks. (*B*) Theoretical predictions of the flow order parameter and defect density plotted as a function of disk size for dimensionless activity α = 10. The onset of circular flows is tightly coupled to the increase of the defect density. Error bars represent SE with $n = T/\tau$ measurements, where T is the simulation duration and τ is the average lifetime of a defect. Below a dimensionless diameter of $\sim$8, theory predicts a transition to a noncirculating ($\langle |\Phi| \rangle_t = 0$) state (21).

density and the flow order parameter change with the confinement size (21). Theory predicts that the onset of the circular flows coincides with the increase in the effective defect density (Fig. 6*B*). Equivalently, circular flows appeared only when the system was confined below the defect spacing preferred by the bulk samples. Increasing the confinement size to the point where any additional defects appear immediately suppressed circular flows. This is in contrast to experiments where active nematics exhibited robust circular flows even in the presence of several additional defect pairs. Thus, theory predicts that the transition to bulk dynamics occurs by a one-step transition characterized by concomitant changes in the defect density and the flow order, while, in the experiment, the structural and dynamic transitions occur for different confinements.

We examined an additional structural aspect of confined active nematics by plotting the time-averaged radial distribution of $+1/2$ defect density for different confinement sizes (Fig. 7*A*). For moderately confined active nematics, the topological constraints gave rise to a defect density distribution with a peak at a well-defined radial position. Intriguingly, the radial position of the peak did not significantly change, even as the confinement diameter increased from 100 μm to 300 μm. Beyond this diameter, the peak in the radial density distribution disappeared. This drop coincides with the onset of the weak confinement dynamics in which defects proliferate (Fig. 5). In this regime, the measured probability distribution was flat within the interior of the disk, and decayed to almost zero upon approaching the boundary. The theoretical model captures both the sharp peak at strong confinements and the flattening of the distribution as the confinement diameter is increased (Fig. 7*B* and ref. 21). However, the details of the predicted defect distribution diverge subtly from the experiment; theory predicts that the maximum of the distribution moves outward with increasing confinement size, in contrast to experimental observations of a fairly large boundary exclusion zone with low defect density. This suggests that the dynamics that direct the $+1/2$ defects toward the center at intermediate confinement are also relevant for larger diameters, transporting defects toward the interior of the disk.

Examining defect motion subsequent to the boundary nucleation provides some insight into the discrepancy between the theory and experiments. Initially, the instability grows perpendicular to the boundary. In isolation, a nucleated $+1/2$ defect would presumably continue to move toward the confinement center. However, existing circular flows and the associated nematic director field rapidly reorient the newly created defects in the azimuthal direction (Fig. 8). Defects with such alignment generate additional active stresses that further stabilize circular flows. Furthermore, evolving dynamics lead to the creation of a compound defect structure composed of a $+1/2$ defect with a $-1/2$ defect that have substantial lifetime before annealing (t = 153 s Fig. 8 and Movie S7). Together, the defect pair acts as an active wedge that further stabilizes the circular flows.

Noncircular Geometries. So far, we described dynamics of circularly confined active nematics. However, the developed experimental methods are more general and can be used to study dynamics in diverse confined geometries. To demonstrate their versatility, we confined active nematics within a disk with an inward notch, an annulus, and rectangular boxes of different lengths and widths. A chiral notch at the confining boundary of a disk controls the spatial location of defect nucleation (Movie S8). It also ensures that autonomous flows have only one handedness, which is reminiscent of the methods that control the flow of confined 3D isotropic active fluids (31). Our experiments showed that confining active nematics within an annulus provides an alternate method of engineering coherent long-ranged flows

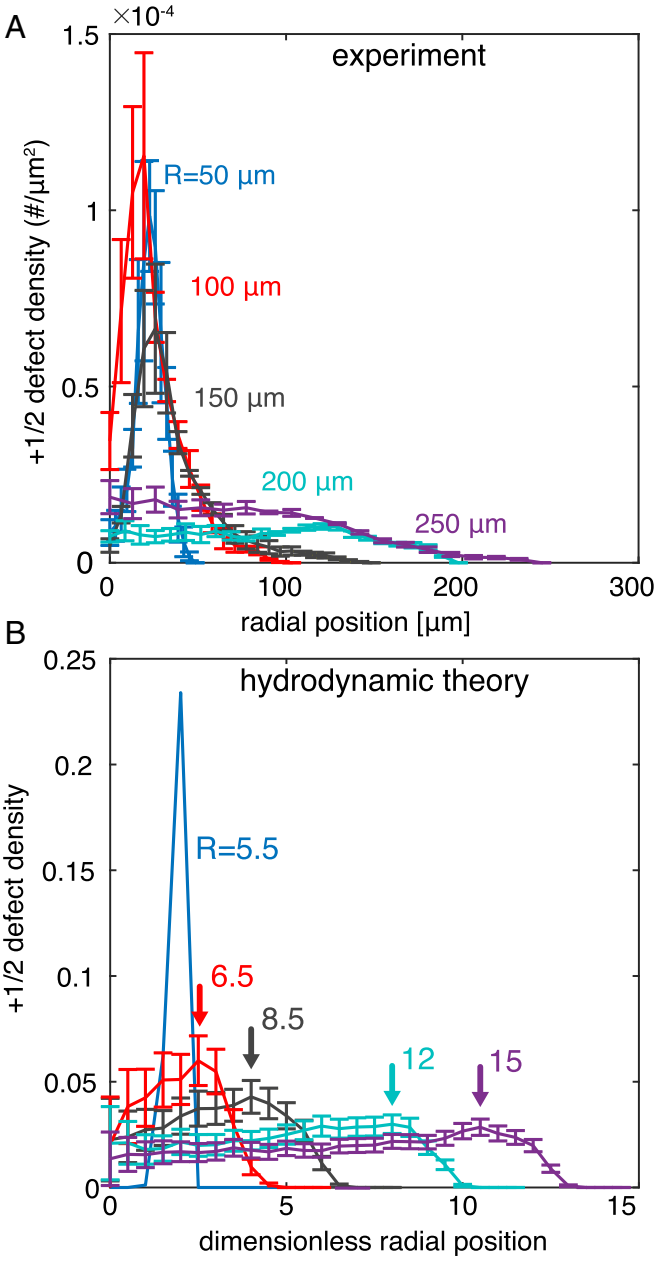

Fig. 7. Radial distribution of defect densities across different confinement regimes. (*A*) Time-averaged radial distributions of $+1/2$ defects plotted for confinements of different radii. For stronger confinements, the topological constraint requires the presence of two $+1/2$ defects regardless of the energetic penalty, giving rise to a sharp peak in the defect density distribution at a well-defined radius. Error bars represent SE across different disks. (*B*) Theoretically calculated defect distribution plotted as a function of confinement size for dimensionless activity α = 10. In small-diameter disks, defects orbit at a preferred radius. In larger-diameter disks, defects tend toward uniform density in the disk interior, with a local maxima (arrows) near the hard wall boundary (21). Error bars represent SE with $n = T/\tau$ measurements, where T is the simulation duration and τ is the average defects lifetime.

(Fig. 9*A* and Movie S9). It remains an important question to determine how the annular width and curvature determines the structure of the self-organized flows. We also observed intriguing dynamics in active nematics confined within a rectangular box with a large aspect ratio (Fig. 9*B* and Movie S10). For the majority of the time, the dynamics of this system are chaotic. However, occasionally, we observed an organized state in which defects

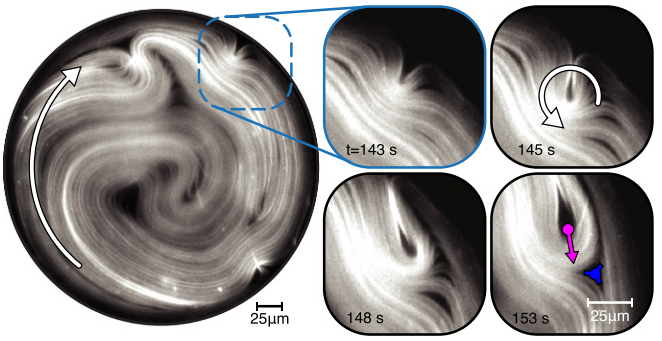

Fig. 8. Dynamics of boundary-nucleated defects. Structure of circularly confined defect-laden active nematic in a weak confinement regime (Movie S7). Enlargements show sequence of images showing a boundary-induced defect nucleation and its subsequent rotation and alignment with the existing director field that reinforces the circular flow. Such dynamics produce long-lived compound $\pm\frac{1}{2}$ pairs featuring a $+1/2$ defect that pushes its oppositely charged counterpart for a substantial time before annealing. Confining diameter is 300 μm.

collectively and simultaneously nucleated at the boundary and subsequently propagated into the interior.

Discussion and Conclusion

Persistent circular motion has been observed in a wide range of confined active matter systems ranging from clusters of motile eukaryotic cells, and dense bacterial suspensions, to synthetic motile colloids (27, 31, 38–41). All of these systems are characterized by a single time scale related to the frequency of the rotational dynamics. Our observations confirm the universality of circular flows in the confined active matter. However, compared with previous experiments and to theoretical predictions, we observed two ubiquitous yet unexplained phenomena. First, in the intermediate confinement regime, the nematic director field formed a double spiral that evolved over time through the multiple procession cycles of $+1/2$ defects. The slow collapse of the $+1/2$ defect orbits drove the system toward a tightly wound, nearly circularly symmetric configuration. Once sufficiently circular, the material was reconfigured by a boundary-induced defect nucleation, initiating a subsequent cycle of the doubly periodic dynamics. Second, as a function of the increasing diameter, we observed a two-step transition from the doubly periodic dynamics to bulk turbulence. Increasing confinement beyond a critical diameter led to a profusion of additional defects that nucleated both at the boundary and within the interior. The density of defects approached the value measured in bulk materials, yet flows remained ordered. Circular flows ceased and bulk chaotic dynamics emerged only after increasing confinement diameter further to the second larger value.

Existing continuum theories of active nematics predict suppression of spontaneous flows below a critical length scale and activity threshold, density flux from high to low director curvature, and chaotic dynamics at high activity and large length scales, and predict regular circulating flows in the intermediate regime (7, 21–26, 42). While these models are not identical, nor are the applied boundary conditions, they all fail to predict both the doubly periodic dynamics at intermediate confinement and the two-step route to bulk-like turbulence. Agent-based models of active nematics might overcome limitations of continuum models by explicitly modeling particle–particle interactions; these models predict buckling instabilities that produce motile defects (15, 43–45) but have not considered the impact of boundary conditions essential for reproducing experimental observations.

Dynamics similar to those described here have been observed in active nematics assembled on smectic focal conic domains which provide soft circular confinement (32). In both cases, there is pronounced migration of microtubules from the high-curvature interior to the lower-curvature boundaries. However, the dynamics that disrupt the circular structure in the two systems are distinct. The smectic-confined circular nematics lose stability along the entire periphery with a well-defined wavelength. In contrast, the hard wall boundary prevents outward buckling, causing nucleation to occur as a distinct, spatially localized event that produces a single $\pm\frac{1}{2}$ defect pair.

Experiments suggest two possible mechanisms that control the doubly periodic dynamics. One possibility is that the buildup of the microtubule density at the boundary increases local active stresses. Once these reach a critical magnitude, the generic nematic instability develops, leading to boundary-induced defect formation. Another possibility is that the defect nucleation is suppressed by the persistent circulating flows that tend to align the director azimuthally. As the defects wind the double spiral tighter, there is a marked decrease in the total active force generated in the azimuthal direction, which leads to the slowdown of the associated flows. Once they decrease below a certain threshold, the flows no longer suppress defect nucleation. This disinhibition initiates another cycle of defect dynamics. These two mechanisms are not mutually exclusive; both increased

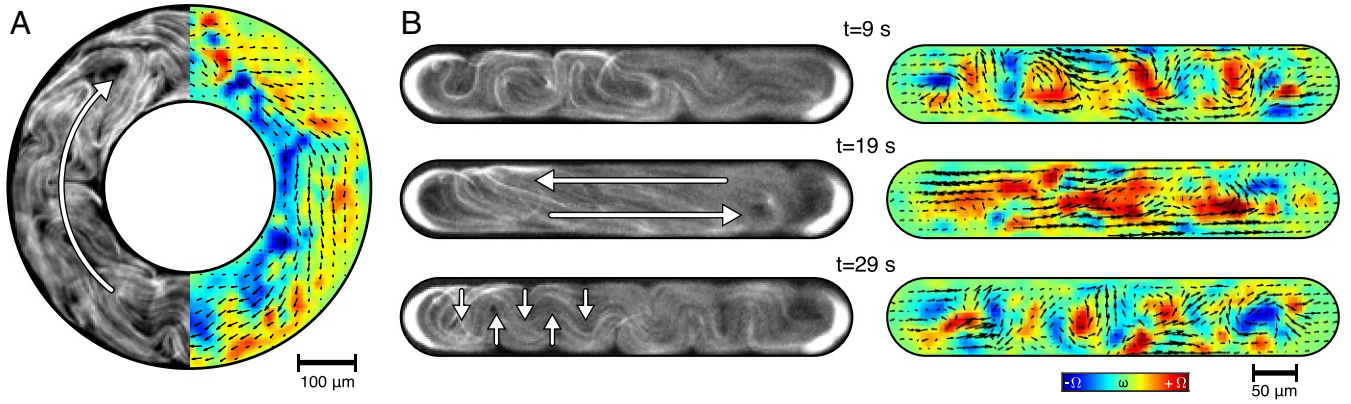

Fig. 9. Active nematics in complex geometries. (*A*) Active nematic confined in a 150-μm-wide annulus. Fluorescently labeled microtubules are shown on the left, and the flow and vorticity field extracted from the PIV analysis is shown on the right (vorticity scale is $\Omega = \pm 0.3\ s^{-1}$). Temporal evolution is shown in Movie S9. (*B*) Active nematic dynamics in rectangular confinements. (Left) Evolving structure of the nematics field. (*Right*) Velocity field and the destruction and re-creation of a single row of vortices with alternating sign (vorticity scale is $\Omega = \pm 0.4\ s^{-1}$). Temporal evolution is shown in Movie S10.

activity and weakened suppression of defect nucleation could be experimentally relevant to controlling the temporal onset of boundary-induced defect nucleation events.

Our observations of defect dynamics further suggest that microtubule-based active nematics are composed of continuous material lines that can be distorted but not crossed by defects. This is evidenced by defect reorientation dynamics (Figs. 2*A* and 8). Driven by molecular activity, the nematic undergoes volume-conserving extension along the director field and contraction in the direction perpendicular to the nematic field (cyan line in Fig. 2*A*). In general, an active $+1/2$ defect can move forward through two mechanisms: one that involves no net material transport but local reorientation of the nematic director field (Fig. 10*A*) and one that requires active expulsion of material in front of the defect along the director field (Fig. 10*B*). The former, while realizable in thermotropic liquid crystals and perhaps even bacterial active nematics (44), is suppressed by the long constituents of the microtubule active nematic. Given the constraints imposed by the director-defined material lines, we observe a preference for the latter mechanism. Similar considerations are also important for the mechanisms of defect annihilation. In low molecular weight nematics, simple reorientation of the nematic director can lead to defect annihilation. In contrast, in microtubule active nematics, the filaments between the annihilating defects have to be expelled through active transport of constituent fibers driven by extensional flows. This might explain the long-lived nature of compound defect pairs (t = 153 s, Fig. 8). Current continuum liquid crystal models lack the constraints on material motion needed to predict the observed defect interactions (5, 9, 46, 47).

In summary, we demonstrated that confinement effectively transforms the chaotic dynamics of bulk 2D active nematics in multiple ways, inducing the formation of self-organized doubly periodic spatiotemporal patterns. These observations pave the way to controlling dynamics of active nematics by tuning the confinement geometry. However, predictive control of the emergent patterns requires both further experimental explorations and development of theoretical models that more accurately account for the experimental realities of defect nucleation and interactions. More broadly, the dynamics of our reconstituted minimal system are evocative of the phenomena observed in living organisms, which frequently exhibit complex spatiotemporal patterns that emerge on length scales and time scales that are significantly larger than the size and the lifetime of the biochemical constituents (48). Using kinesin motors that take an 8-nm-sized step every 10 ms, we demonstrated self-organized spatiotemporal patterns with lifetimes of minutes on length scales of hundreds of microns. Understanding the fundamental organizing principles that drive the dynamics of active nematics might reveal general strategies for rationally engineering adaptable and dynamical synthetic materials with biomimetic capabilities.

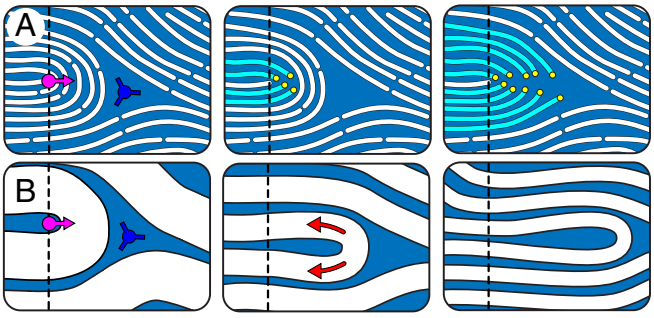

Fig. 10. Mechanisms of defect propulsion and annihilation: In the microtubule, active nematic defect propulsion can occur through a combination of thinning and fracture mechanisms. (*A*) Constituent fibers reorient and fracture, allowing the $+1/2$ defect core to move forward. The fracture-driven motility does not require material transport. (*B*) In the regime where constituents cannot easily reorient, ordered fibers lying in front of the $+1/2$ defect prevent its forward movement. Extensile active transport within the nematic along director lines (red arrows) causes elongation and thinning that both propels the defect pair forward and brings them closer together. Their annihilation rate is limited by the rate at which the extensile flows can displace the materials in front of the $+1/2$ defect. Dashed line indicates the initial defect position.

Methods

Microtubule-Based Active Nematics. We used active nematics comprising three components: GMPCPP stabilized microtubules with an exponential length distribution with a mean of 1 μm to 2 μm (15, 17) labeled with Alexa 647 dye, biotin-labeled kinesin motors bound into multimotor clusters by tetrameric streptavidin (49), and a depletion agent, poly(ethylene glycol), that induces microtubule bundling while still allowing for the microtubules' relative sliding (50–52). The composition and preparation of the active mixture is the same for all experiments. Kinesin clusters simultaneously bind multiple microtubules in a bundle and, depending on their relative polarity, drive the bundle extension (14). Purified microtubules were flash-frozen, stored at −80 °C, and rapidly thawed before use; they were kept at room temperature (20 °C to 25 °C) throughout the experiment. Following previous work, we sedimented the extensile bundles onto a surfactant stabilized oil–water interface, where they assemble into a dense quasi-2D active nematic film. The aqueous suspension also contained an ATP-regenerating system, to increase the experimental lifetime, and an antioxidant system, to prevent photobleaching (14, 15). Depending on the source of the kinesin motor proteins and microtubules, the dynamics of active nematic can vary significantly. Similarly, we found that these parameters greatly affected the frequency of circulating active nematics. However, they did not affect the confinement size where dynamics transitions between strong, intermediate and weak regimes.

Fabricating Microchambers for Confinement. An array of circular microchambers with diameters that ranged from 60 μm to 800 μm were fabricated on glass microscope slides using standard photolithography techniques (Fig. 1*A*). The 3 × 4 inch microscope glass slides were precut to 3 × 3 inches using a diamond tip scriber, to fit them in the vacuum chuck of the mask aligner. The slides were then rinsed and sequentially sonicated (*i*) with hot water containing 0.5% detergent (Hellmanex III; Hellma Analytics), (*ii*) then with ethanol, and (*iii*) finally with 0.1 M NaOH. To enhance SU8 bonding to glass, the slides were immersed in a silane mixture consisting of 98% deionized water, 1% acetic acid, and 1% (3-aminopropyl) trimethoxysilane (Sigma Aldrich) for 20 min. Slides were then rinsed with deionized water, dried with N_2 gas, and placed on a hot plate at 180 °C for 15 min to remove moisture. Once cooled, photoresist SU8 3025 (MicroChem Corp.) was spin-coated on the slides at 1,400 rpm (Headway Research). Subsequent standard photolithography processing steps, including soft-baking for 20 min at 95 °C, UV exposure through a photomask with 180 mJ/cm^2 and postexposure baking for 10 min at 95 °C. Photoresist development was carried out on the slides, followed by hard-baking for 30 min at 180 °C. The depth of the microchambers was ∼30 μm as measured by an optical profilometer.

Assembling the Flow Cell and Confining the Active Nematics. To prevent nonspecific adsorption of microtubules and motors and to create a hydrophilic surface, the lithographed microscope glass slides and no. 1.5 coverslips were plasma-etched and coated with polyacrylamide as described elsewhere (53). Subsequently, each slide was rinsed and dried with N_2 gas immediately before use. Polyacrylamide-treated lithographed slides and cover slips were assembled into a flow cell using ∼100-μm-thick double-sided transfer tape (3M 93005LE) with laser-cut flow channels. HFE7500 oil (3M) with 1.8% (v/v) Fluoro-surfactant (RAN Biotechnologies) was flowed into the cell. Subsequently, the aqueous active mixture was flowed through the channel, displacing the oil–surfactant mixture from all but the hydrophobic SU8 microchambers. The flow channel was then sealed with optical UV-curable glue and centrifuged at 215 × g for 10 min using a Sorval Legend RT (rotor 6434) to drive the bundled microtubules onto the surfactant-stabilized oil–water interface. Within each sample, on average, about 20% of disks had well-defined circularly confined active nematic. Fluorinated oil often wetted areas of the SU8 photoresist, leading to the regions that formed bulk-like unconfined active nematics. However, since there were several hundred

microchambers per slide and less than 10 could be imaged during the lifetime of the active nematic, the 20% success rate was sufficient.

Imaging Confined 2D Active Nematic. The confined active nematic was imaged using a wide-field fluorescent Nikon Eclipse Ti-E microscope with an Andor Clara camera controlled by Micromanager open-source software. The dynamics of quasi-2D active nematics is dependent on the thickness and concentration of microtubule film, the product of which is proportional to the optical retardance, which was determined with an LC-PolScope module (15). Birefringence of the SU8 photoresist limited our ability to quantify the retardance of the confined active nematic. To avoid spillover of signal from the SU8 periphery, the field aperture was partially closed to image about three-quarters of the confined area. These measurements determined the upper bound of the retardance of the nematic to be about a nanometer, which is close to the retardance resolution limit. Because of the small ratio of signal to noise, we could not quantitatively compare the retardance of the contents of the disks across experiments.

Image Processing of the Director Field. In contrast to previous studies, the high birefringence of SU8 photoresists precludes the use of the LC-PolScope to directly quantify the director field (15). Instead, the director field was extracted from fluorescence images. The nematic order tensor, $\mathbf{Q} = \mathbf{n} \otimes \mathbf{n} - 1/2\mathbf{I}$, was constructed by finding the direction $\mathbf{n}$, perpendicular to the principal direction of the structure tensor of the image $\nabla I \otimes \nabla I$, where I is image intensity pixel value (16). The degree of order, $s = 2\mathrm{Tr}\langle \mathbf{Q} \rangle^2$, was found by averaging $\mathbf{Q}$ over a small region. To avoid assigning nematic order to regions that are largely devoid of microtubules, the displayed scalar order parameter field S was weighted by the image intensity (I) if the pixel value was below 10% of the maximum ($I_{\max}$); $S = s * I/I_{\max}$, with s as the unweighted order parameter. Defects in the director field were found using a previously developed algorithm (15). Defect tracking errors for the dataset represented in Fig. 5 are shown in *SI Appendix*, Fig. S2.

Processing of the Flow Field. The velocity field $\mathbf{u}$ was found by applying particle image velocimetry analysis to the fluorescently labeled microtubules using the MatLab plug-in PIVlab v1.43 (54). In typical PIV applications, the flow is quantified by following sparsely labeled, small, isotropic tracer particles. Since these conditions would decrease the quality of the measured director field, PIV analysis is performed on densely labeled microtubules. Consequently, velocity components parallel to the director are undersampled. For example, since the nematic is nearly parallel along the boundaries, we expect the PIV analysis to underestimate the tangential flows in these regions and, consequently, the order of tangential flow ordering $\Phi = \langle \mathbf{u} \cdot \hat{\mathbf{e}}_\theta / |\mathbf{u}| \rangle$ discussed in the text. We were still able to detect circulation in many cases because $+1/2$ defects dominate motion. They feature a nematic field perpendicular to the direction of their motion, which is well captured by the PIV algorithm.

ACKNOWLEDGMENTS. We acknowledge useful conversations with Michael Hagan, Aparna Baskaran, and Stephen DeCamp. Experimental work on circular confinements was supported by Department of Energy of Basic Energy Sciences, through Award DE-SC0010432TDD. Development of the microfluidic confinement technology and extension to noncircular geometries was supported by the Brandeis Materials Research Science and Engineering Center (MRSEC) through Grant NSF-MRSEC-1420382. We also acknowledge the use of the MRSEC optical, microfluidic, and biosynthesis facility supported by Grant NSF-MRSEC-1420382. Development of the computational model of confined active nematics was supported by Grant NSF-DMR-1810077.

1. Aditi Simha R, Ramaswamy S (2002) Hydrodynamic fluctuations and instabilities in ordered suspensions of self-propelled particles. *Phys Rev Lett* 89:058101.
2. Marchetti MC, et al. (2013) Hydrodynamics of soft active matter. *Rev Mod Phys* 85:1143–1189.
3. Ramaswamy S (2010) The mechanics and statistics of active matter. *Annu Rev Condens Matter Phys* 1:323–345.
4. Shelley MJ (2016) The dynamics of microtubule/motor-protein assemblies in biology and physics. *Annu Rev Fluid Mech* 48:487–506.
5. Giomi L, Bowick MJ, Ma X, Marchetti MC (2013) Defect annihilation and proliferation in active nematics. *Phys Rev Lett* 110:228101.
6. Thampi SP, Golestanian R, Yeomans JM (2014) Instabilities and topological defects in active nematics. *Europhys Lett* 105:18001.
7. Gao T, Blackwell R, Glaser MA, Betterton MD, Shelley MJ (2015) Multiscale polar theory of microtubule and motor-protein assemblies. *Phys Rev Lett* 114: 048101.
8. Giomi L (2015) Geometry and topology of turbulence in active nematics. *Phys Rev X* 5:031003.
9. Shankar S, Ramaswamy S, Marchetti MC, Bowick MJ (2018) Defect unbinding in active nematics. arXiv:1804.06350.
10. Thampi SP, Golestanian R, Yeomans JM (2013) Velocity correlations in an active nematic. *Phys Rev Lett* 111:118101.
11. Oza AU, Dunkel J (2016) Antipolar ordering of topological defects in active liquid crystals. *New J Phys* 18:93006.
12. Narayan V, Ramaswamy S, Menon N (2007) Long-lived giant number fluctuations in a swarming granular nematic. *Science* 317:105–108.
13. Zhou S, Sokolov A, Lavrentovich OD, Aranson IS (2014) Living liquid crystals. *Proc Natl Acad Sci USA* 111:1265–1270.
14. Sanchez T, Chen DTN, Decamp SJ, Heymann M, Dogic Z (2012) Spontaneous motion in hierarchically assembled active matter. *Nature* 491:431–434.
15. DeCamp SJ, Redner GS, Baskaran A, Hagan MF, Dogic Z (2015) Orientational order of motile defects in active nematics. *Nat Mater* 14:1110–1115.
16. Ellis PW, et al. (2018) Curvature-induced defect unbinding and dynamics in active nematic toroids. *Nat Phys* 14:85–90.
17. Guillamat P, Ignés-Mullol J, Sagués F (2016) Control of active liquid crystals with a magnetic field. *Proc Natl Acad Sci USA* 113:5498–5502.
18. Luo Y, et al. (2016) Around the corner: Colloidal assembly and wiring in groovy nematic cells. *Phys Rev E* 93:032705.
19. Senyuk B, et al. (2013) Topological colloids. *Nature* 493:200–205.
20. Peng C, et al. (2016) Control of colloidal placement by modulated molecular orientation in nematic cells. *Sci Adv* 2:e1600932.
21. Norton MM, et al. (2018) Insensitivity of active nematic liquid crystal dynamics to topological constraints. *Phys Rev E* 97:012702.
22. Woodhouse FG, Goldstein RE (2012) Spontaneous circulation of confined active suspensions. *Phys Rev Lett* 109:168105.
23. Shendruk TN, Doostmohammadi A, Thijssen K, Yeomans JM (2017) Dancing disclinations in confined active nematics. *Soft Matter* 13:3853–3862.
24. Gao T, Betterton MD, Jhang AS, Shelley MJ (2017) Analytical structure, dynamics, and coarse graining of a kinetic model of an active fluid. *Phys Rev Fluids* 2:093302.
25. Theillard M, Alonso-Matilla R, Saintillan D (2017) Geometric control of active collective motion. *Soft Matter* 13:363–375.
26. Chen S, Gao P, Gao T (2018) Dynamics and structure of an apolar active suspension in an annulus. *J Fluid Mech* 835:393–405.
27. Wioland H, Woodhouse FG, Dunkel J, Kessler JO, Goldstein RE (2013) Confinement stabilizes a bacterial suspension into a spiral vortex. *Phys Rev Lett* 110:268102.
28. Lushi E, Wioland H, Goldstein RE (2014) Fluid flows created by swimming bacteria drive self-organization in confined suspensions. *Proc Natl Acad Sci USA* 111:9733–9738.
29. Segerer FJ, Thüroff F, Piera Alberola A, Frey E, Rädler JO (2015) Emergence and persistence of collective cell migration on small circular micropatterns. *Phys Rev Lett* 114:228102.
30. Wioland H, Lushi E, Goldstein RE (2016) Directed collective motion of bacteria under channel confinement. *New J Phys* 18:27–30.
31. Wu KT, et al. (2017) Transition from turbulent to coherent flows in confined three-dimensional active fluids. *Science* 355:eaal1979.
32. Guillamat P, Ignés-Mullol J, Sagués F (2017) Taming active turbulence with patterned soft interfaces. *Nat Commun* 8:564.
33. Kamien RD (2002) The geometry of soft materials: A primer. *Rev Mod Phys* 74:953–971.
34. Gârlea IC, et al. (2016) Finite particle size drives defect-mediated domain structures in strongly confined colloidal liquid crystals. *Nat Commun* 7:12112.
35. Duclos G, Erlenkämper C, Joanny JF, Silberzan P (2017) Topological defects in confined populations of spindle-shaped cells. *Nat Phys* 13:58–62.
36. Putzig E, Baskaran A (2014) Phase separation and emergent structures in an active nematic fluid. *Phys Rev E Stat Nonlin Soft Matter Phys* 90:042304.
37. Lemma LM, Decamp SJ, You Z, Giomi L, Dogic Z (2018) Statistical properties of autonomous flows in 2D active nematics. arXiv:1809.06938.
38. Doxzen K, et al. (2013) Guidance of collective cell migration by substrate geometry. *Integr Biol* 5:1026–1035.
39. Bricard A, Caussin JB, Desreumaux N, Dauchot O, Bartolo D (2013) Emergence of macroscopic directed motion in populations of motile colloids. *Nature* 503:95–98.
40. Bricard A, et al. (2015) Emergent vortices in populations of colloidal rollers. *Nat Commun* 6:7470.
41. Tee YH, et al. (2015) Cellular chirality arising from the self-organization of the actin cytoskeleton. *Nat Cel Biol* 17:445–457.
42. Putzig E, Redner GS, Baskaran A, Baskaran A (2016) Instabilities, defects, and defect ordering in an overdamped active nematic. *Soft Matter* 12:3854–3859.
43. Joshi A, Putzig E, Baskaran A, Hagan MF (2019) The interplay between activity and filament flexibility determines the emergent properties of active nematics. *Soft Matter* 15:94–101.
44. Li H, et al. (2018) Data-driven quantitative modeling of bacterial active nematics. *Proc Natl Acad Sci USA* 33:777–785.
45. Yaman YI, Demir E, Vetter R, Kocabas A (2018) Emergence of active nematics in bacterial biofilms. arXiv:1811.12076. Preprint, posted November 29, 2018.
46. Tang X, Selinger JV (2018) Theory of defect motion in 2D passive and active nematic liquid crystals. *Soft Matter* 15:587–601.
47. Cortese D, Eggers J, Liverpool TB (2018) Pair creation, motion, and annihilation of topological defects in two-dimensional nematic liquid crystals. *Phys Rev E* 97:1–10.
48. Brugués J, Needleman D (2014) Physical basis of spindle self-organization. *Proc Natl Acad Sci USA* 111:18496–18500.
49. Nedelec F, Surrey T, Maggs AC, Leibler S (1997) Self-organization of microtubules and motors. *Nature* 389:305–308.

50. Needleman DJ, et al. (2004) Synchrotron x-ray diffraction study of microtubules buckling and bundling under osmotic stress: A probe of interprotofilament interactions. *Phys Rev Lett* 93:198104.
51. Hilitski F, et al. (2015) Measuring cohesion between macromolecular filaments one pair at a time: Depletion-induced microtubule bundling. *Phys Rev Lett* 114:138102.
52. Ward A, et al. (2015) Solid friction between soft filaments. *Nat Mater* 14:583–588.
53. Lau A, Prasad A, Dogic Z (2009) Condensation of isolated semi-flexible filaments driven by depletion interactions. *Europhys Lett* 87:48006.
54. Thielicke W, Stamhuis EJ (2014) PIVlab–Towards user-friendly, affordable and accurate digital particle image velocimetry in MATLAB. *J Open Res Softw* 2:e30.